GEOPHYSICS

Wide-angle seismic reflections reveal a lithosphere-asthenosphere boundary zone in the subducting Pacific Plate, New Zealand

Pasan Herath[1]*, Tim A. Stern[1], Martha K. Savage[1], Dan Bassett[2], Stuart Henrys[2]

New wide-angle seismic reflection data from offshore New Zealand show that the lithosphere-asthenosphere boundary (LAB) is more structured than previously thought. Three distinct layers are interpreted within a 10- to 12-km-thick LAB zone beginning at a depth of ≈70 km: a 3 (±1)–km-thick layer at the bottom of the lithosphere with a P-wave (V_P) azimuthal anisotropy of 14 to 17% and fast azimuth subparallel to the direction of absolute plate motion and a 9 (±2)–km-thick, low V_P channel with a P-wave–to–S-wave velocity ratio (V_P/V_S) of >2.8 in the upper 7 km of the channel and 1.8 to 2.6 in the lower 2 km of the channel. The high V_P/V_S ratios indicate that this channel may contain 3 to 20% partial melt that facilitates decoupling of the lithosphere from the asthenosphere and reduces resistance for plate motion. Furthermore, the strong azimuthal anisotropy above the low-velocity layer suggests localization of strain due to melt accumulation.

INTRODUCTION

A key requirement for plate tectonics is that there is limited resistive drag for lithospheric plates to move over the asthenospheric mantle (1). Yet, imaging and understanding the mechanical nature of the lithosphere-asthenosphere boundary (LAB) has been a long-standing challenge to seismology (2). The LAB was viewed as a staggered zone separating solid-state convective heat transfer in the asthenosphere from solid-state thermal conduction through the lithosphere. It was in keeping with a long-standing intuition that the lithosphere is in effect a thermal boundary layer of mantle convection. Lithospheric thickening with age, and rheology (e.g., viscosity) and creep mechanism changing with depth suggest that temperature plays a dominant role in controlling the depth of the LAB (2–4), further corroborating the thermal notion of the LAB.

Much of the inference about the structure of the LAB is based on passive-source seismic methods with either surface or body waves (5–7). These data typically have frequencies less than 1 Hz, resulting in seismic wavelengths greater than 10 km. The technical difficulty in determining fine structures at shorter length scales has likely contributed to the view that the LAB is a diffusive boundary with a length scale of 10 km or greater (2, 5). However, actual depths of the LAB within a given age interval have been found to deviate significantly from those predicted from thermal models (3), implying that temperature solely cannot be used to explain the LAB.

Recent receiver function studies have shown that the LAB is sharper than a thermal boundary layer, with thicknesses ranging from 11 to 15 km with a 3 to 15% drop in shear-wave velocity (6, 8, 9). However, detailed structure within the LAB on a scale less than 10 km cannot be resolved with 1-Hz passive-source seismic data. More recently, controlled-source seismic methods have been applied to image the LAB under oceanic plates at subduction and mid-oceanic ridge settings, and a different nuance on its structure is emerging (10, 11). These data, with dominant frequencies of 4 to 14 Hz, are near vertical reflection images from both large explosion and airgun sources. They reveal several coherent reflective horizons that can be tracked continuously for distances up to 200 km at LAB depths (70 to 100 km). On the basis of polarity and amplitudes, these reflections are interpreted to define a ≈10-km-thick LAB channel with a P-wave velocity drop of ≈10%. This velocity drop at the LAB has been linked to the presence of partial melt or volatiles (6, 8, 9) that would effectively facilitate the decoupling of the lithosphere from the asthenosphere. This is necessary for plate tectonics to occur. In addition to seismic data, magnetotelluric imaging also reveals the presence of a partially molten layer with high electrical conductivity at LAB depths in both subduction (12) and mid-oceanic ridge (13) settings. Both seismic and magnetotelluric data further reveal that, with increasing plate age, the thickness of the melt channel appears to reduce and the depth of the channel appears to increase (11, 13), although with some local variability (3). These studies also suggest that the melt channel may be common but not necessarily a pervasive feature.

In this study, we advance the investigation of the fine structure of the LAB one step further. We interpret the LAB at the Hikurangi subduction zone in New Zealand where the Pacific Plate dives beneath the Australian Plate (Fig. 1A). Here, subduction of the Hikurangi oceanic plateau occurs despite the extra buoyancy provided by the thicker (10 to 12 km) (14, 15)-than-normal (6 to 8 km) oceanic crust. We analyze wide-angle reflections generated by offshore airgun sources and subsequently recorded by seismographs onshore (16). This dataset was acquired during the Seismic Array HiKurangi Experiment (SAHKE) in 2009–2010 (Fig. 1B) (15). This onshore-offshore technique has added advantages over ocean bottom seismographs in investigating the LAB as there is more control to place seismographs on firm bedrock with improved sensor coupling to the ground. Moreover, wide-angle reflections provide enhanced amplitudes as the incidence angle approaches the critical angle (typically >55°) (17). This is a key property because there are some impedance contrasts that only generate significant amplitudes at these wide angles and are essentially hidden from near vertical reflection surveys.

[1]Institute of Geophysics, Victoria University of Wellington, Wellington, New Zealand. [2]GNS Science, Lower Hutt, New Zealand.
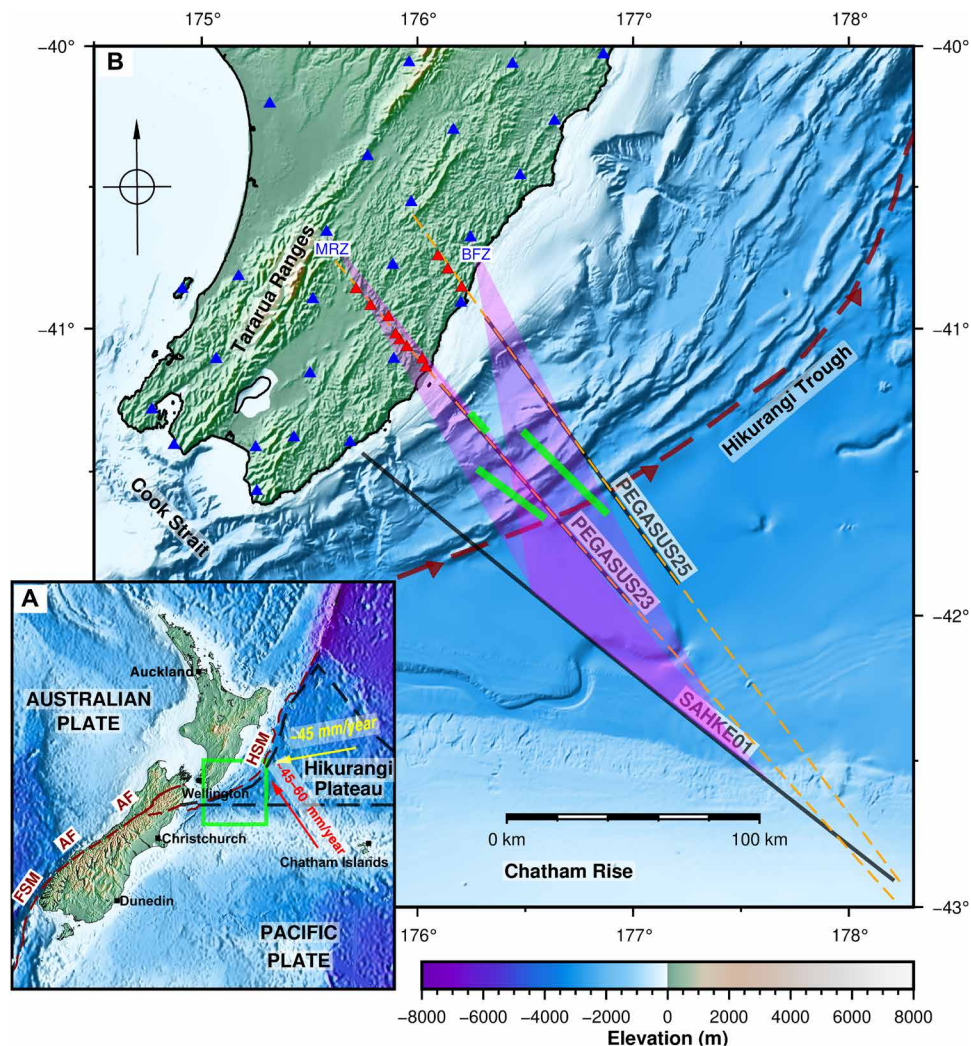*Corresponding author. Email: pasansherath@gmail.com

Fig. 1. Tectonic setting around New Zealand and the study area. (**A**) Tectonic setting around New Zealand. HSM, Hikurangi subduction margin; AF, Alpine Fault; FSM, Fiordland subduction margin. Colored vectors indicate the absolute plate motion of the Pacific Plate (red) and the plate motion of the Pacific Plate relative to the Australian Plate (yellow). The black dashed line indicates the extent of the Hikurangi oceanic plateau. The green rectangle indicates the extents of (B). (**B**) Study area. Red triangles are temporary seismographs of the PEGASUS23 and PEGASUS25 onshore-offshore transects. Blue triangles are permanent seismographs of the GeoNet network. Black lines are offshore multichannel seismic lines. Orange dashed lines are the extended PEGASUS23 and PEGASUS25 onshore-offshore transects (*14*, *15*). Purple shade indicates the airgun source–onshore receiver swaths of the common receiver gathers used in the study. Thick green lines indicate the spatial locations of the deep reflectors identified in this study.

RESULTS

Onshore-offshore seismic data are viewed as common receiver gathers, which primarily represent the arrival times and the amplitudes of seismic reflections and refractions at a receiver as a function of source-receiver offset. In the common receiver gathers at two permanent seismographs, i.e., BFZ and MRZ, located in the southern Hikurangi margin (Fig. 1B), we observe a band of reflectivity between source-receiver offsets of about 140 to 260 km and two-way travel times of about 30 to 40 s (reduced travel times of about 8 to 13 s at a reduction velocity of 8 km/s) (Fig. 2 and figs. S1 to S3). Within this reflectivity, we identify four distinct wide-angle reflections, i.e., R_0, R_1, R_2, and R_3 (see Materials and Methods). A first-order approximation for the depth of R_0 at zero offset places it at a depth of about 47 km beneath the Moho (absolute depth of about 74 km) (fig. S4), suggesting that

the series of reflections originate from LAB depths of the subducted Pacific Plate.

Across the three common receiver gathers (Fig. 2 and fig. S1), the reflectivity is variable, with the arrivals at onshore station BFZ (Fig. 2A) being the clearest. This is probably a result of high coupling between the sensor and the ground, and its positioning on firm Cretaceous greywackes. An important feature of these wide-angle reflections is their respective shapes, or moveouts (*18*). Two key observations are R_1 appearing to merge with R_0 at offsets between 190 and 200 km at BFZ (Fig. 2A and fig. S2) and the parallelism of R_2 and R_3 events with their immediate predecessors R_1 and R_2, respectively. The observation of similar moveout relationships between these four reflections at the MRZ station (Fig. 2F and fig. S3), despite not being as clear as those at BFZ (Fig. 2A), gives confidence that the reflections (R_0 to R_3) in the two records at BFZ and MRZ
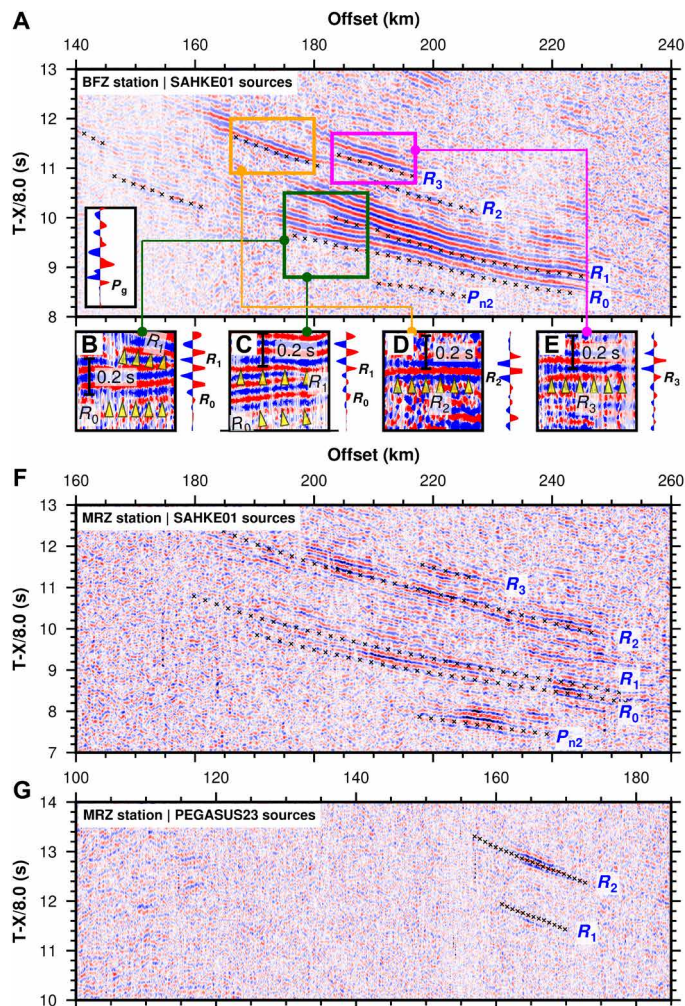
Fig. 2. Late-arriving, wide-angle reflections in common receiver gathers. (**A**) Common receiver gather at the BFZ station with the airgun sources of the SAHKE01 line. Colored rectangles show the regions of (A) used in (B) to (E). The inset in (A) shows the polarity of the first arriving crustal refraction (P_g) at the BFZ station. (**B** to **E**) Stacks of R_0 to R_3 reflections flattened horizontally using the travel time of each reflection at each trace (left) and the stacked trace from the flattened traces (right). Note that for (B) and (C), the same region in (A) is used, but the stacks have been flattened with the travel-time picks of R_0 and R_1, respectively. The interpreted first breaks of the arrivals are also shown as yellow arrows. (**F**) Common receiver gather at MRZ station with airgun sources of the SAHKE01 line. (**G**) Common receiver gather at the MRZ station with airgun sources of the PEGASUS23 line. Black crosses indicate the pick arrivals of R_0 to R_3 reflections.

Fig. 3. One-dimensional velocity model fitting the travel times of R_0 to R_3 reflections. (**A**) One-dimensional velocity model with average P-wave velocities above the R_0 reflector that fits the travel times of R_0 to R_3 reflections observed in Fig. 2A. (**B**) Observed travel times (centered at the gray error bars) and calculated travel times (black curves) for R_0 to R_3 reflections. Colored circles indicate the angle of incidence of the raypaths with offset at R_0 to R_3 reflections.

the travel time within a low velocity layer remain similar with increasing offsets.

Polarity of the first break is also a useful attribute to learn about the impedance contrast associated with a seismic reflection boundary (*19*). From first arriving P_g refractions at BFZ, we calibrate the red pulse to be positive (upward motion) (Fig. 2A). We picked the first breaks of R_0 to R_3 reflections manually by analyzing the continuity of the wave train through the gather in Fig. 2A. Although these deep reflections are emergent in places, our interpretation of the polarity for R_0 to R_3 reflections indicates that R_0, R_1, and R_3 have the first dominant amplitude peak breaking to the right (red pulse) with R_2 having reversed polarity (blue pulse) (Fig. 2, B to E). These observations together with reflection moveouts (Fig. 2) provide the underpinning constraints for building a more specific velocity model for the base of the Pacific Plate.

Previous seismic studies of the Hikurangi margin provide evidence for unusually high P-wave speeds (8.5 to 9.0 km/s) in the upper mantle (*14, 20–22*). In addition to the Hikurangi Plateau, similar high P-wave speeds have been detected under Ontong-Java and Manihiki Plateaus and are linked to the AG fabric (*23*) interpreted to have formed predominantly by uniaxial flattening in a spreading plume head (*20*). The AG fabric in forsterite-rich olivine aggregates is characterized by a girdle of high P- and S-wave speeds (P-wave, ≈8.7 to 8.8 km/s; S-wave, ≈5.1 km/s), with a slower speed orthogonal to this (P-wave, ≈7.8 km/s; S-wave, ≈4.7 km/s) (*20*). We adopt a P-wave speed of 8.7 km/s at a depth of 50 km, based on modeling upper mantle refractions (P_n phases) from the Hikurangi Plateau (*14*). We model the P-wave speed to increase to 8.9 km/s just above the R_0 reflector at a depth of 70 ± 1 km (Fig. 4, A and C, and figs. S6 and S7). With this constraint, our ray trace models require the layer between R_0 and R_1 to be of high velocity (>9 km/s) to replicate R_1 merging with R_0 at offsets between 190 and 200 km (Fig. 2A). Although mantle velocities this high are rarely seen at depths of 70 km, anisotropy of olivine will permit P-wave speeds up to 9.8 km/s if sufficiently high values of finite shear strain have been acquired (*24, 25*).

Two-dimensional (2D) isotropic ray trace models (see Materials and Methods) show that the layer between R_0 and R_1 is consistent with a ≈3-km-thick layer with a P-wave velocity of 9.2 to 9.3 km/s (Fig. 4 and fig. S6). These parameters are further confirmed by 3D

originate from the same structures. Seismic ray trace models indicate that the simplest way of explaining the relationship between R_0 and R_1 is for the intervening layer to be a thin, high–P-wave velocity layer (Fig. 3 and fig. S5) as the transmitted ray from R_0 bends away from the normal before reflecting from R_1, resulting in a decrease of travel-time difference between R_0 and R_1 with increasing source-receiver offset. Thus, the travel-time curve of R_1 appears to merge with that of R_0 with increasing source-receiver offset. In contrast, the mutual parallelism between R_1 and R_2 and between R_2 and R_3 can be explained by low-velocity intervening layers (Fig. 3 and fig. S5) because the transmitted ray from the top bends toward the normal before reflecting up from the base. Thus, the raypath length and
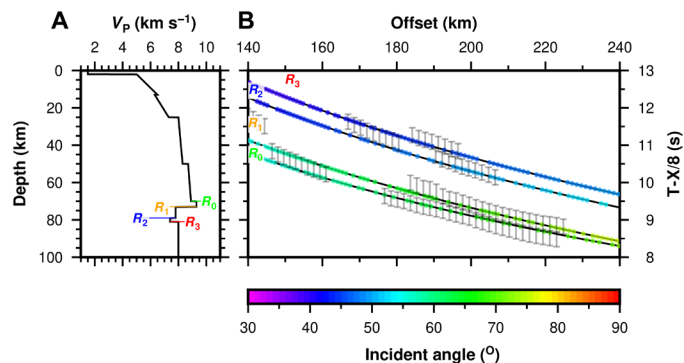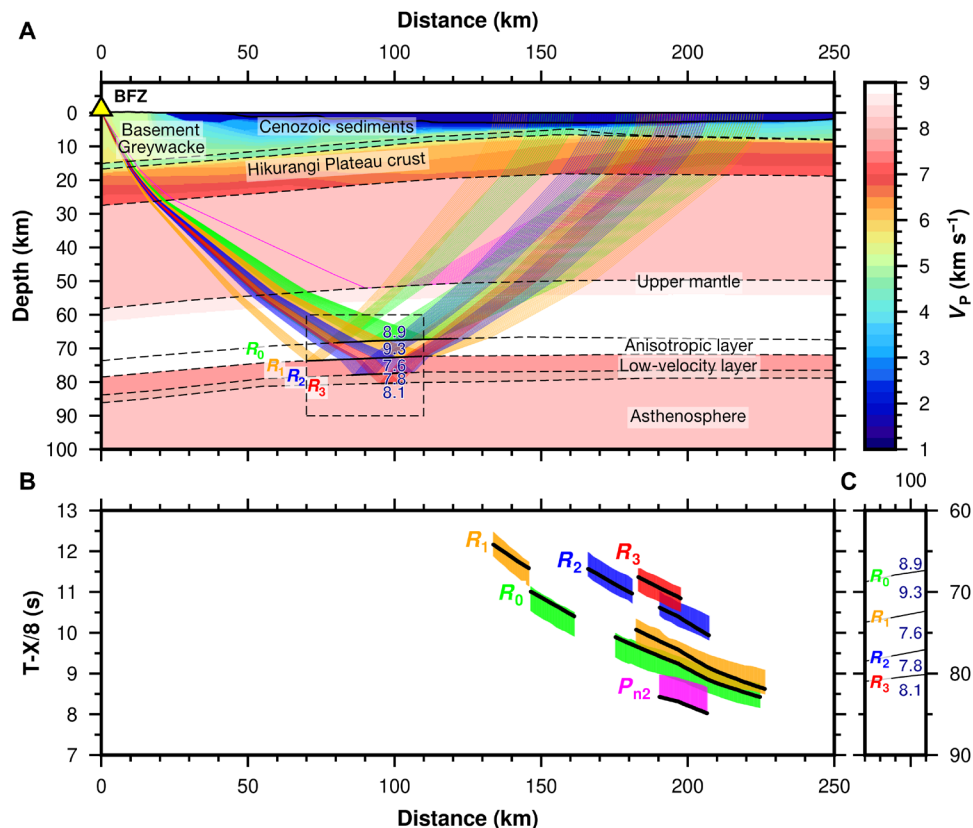
Fig. 4. Two-dimensional isotropic P-wave velocity and ray trace model of the wide-angle reflections at the BFZ station with SAHKE01 airgun sources. (**A**) P-wave velocity model and traced raypaths in two dimensions for the observed wide-angle reflections and refractions recorded at the BFZ station with the airgun sources of the SAHKE01 line (Fig. 2A). (**B**) Travel-time picks of the phases observed in Fig. 2A color-coded as in (A). Height of an observed travel-time pick is twice the pick uncertainty. Calculated travel times are in black. Note that the travel-time axis is reduced with a velocity of 8.0 km/s. (**C**) Enlarged section of P-wave velocities of the region shown by the black, dashed rectangle in (A).

anisotropic ray trace and synthetic seismogram models (see Materials and Methods) that better fit the moveouts of the R_0 and R_1 reflections, which suggest that the layer between R_0 and R_1 is required to be 3 ± 1 km thick and it has a faster P-wave velocity of 9.3 to 9.6 km/s parallel to the layer interface and along an azimuth between 322° and 342° (Fig. 5 and figs. S8 to S19). The P-wave velocity in the vertical direction, approximately perpendicular to the layer interface, is modeled to be 8.3 to 8.5 km/s. These velocity constraints indicate a P-wave anisotropy of 14 to 17% and can replicate the positive polarity of the first break of R_0 reflection (fig. S20A).

The mutually parallel moveouts of R_1 and R_2 suggest that the layer between them is a low–P-wave velocity layer, yet the positive first break of R_1 suggests otherwise (Fig. 2, A and C). However, within the range of incident angles for R_1, the positive first break is consistent with a low–P-wave velocity layer if the V_P/V_S ratio is >2.8 (figs. S20B, S21, and S22). We adopt a P-wave velocity of 7.6 km/s for this layer, similar to the percentage velocity reduction (5 to 12%) associated with other low-velocity layers detected in the oceanic lithosphere (6, 11). The resultant thickness of the layer is 7 ± 2 km from ray tracing (Fig. 4A and figs. S6, S23, and S24A).

Similarly, the mutually parallel moveouts of R_2 and R_3 suggest that the layer between them has a low P-wave velocity. Furthermore, we interpret the R_2 reflection to have a negative polarity (Fig. 2D). Assuming a maximum 12% velocity reduction, the P-wave velocity of

this layer could range between 7.1 and 8.1 km/s. These polarity and P-wave velocity constraints are consistent with a 2 (±1)–km-thick layer (fig. S24B). V_P/V_S ratio estimates for this layer can range from 1.8 to 2.6 based on amplitude versus offset (AVO) modeling (see Materials and Methods) that would result in a weak negative polarity for the reflection coefficients (fig. S25). The R_3 reflector has an interpreted positive polarity (Fig. 2E) and the layer beneath is assumed to be regular asthenosphere with a P-wave velocity of 8.1 km/s and a V_P/V_S ratio of 1.8 (26).

The synthetic common receiver gather computed for BFZ station that accounts for the 3D source-receiver raypath geometry (see Materials and Methods) resembles the observed common receiver gather and is consistent with the travel times, moveouts, and first break polarities of R_0 to R_3 reflections (Fig. 5, C to G). Our synthetic data do not, however, account for the apparent drop-off of reflectivity for offsets >230 km observed in the data (Fig. 2A). This may be a result of lateral variation in attenuation, noise, or material properties.

We interpret R_0, R_1, R_2, and R_3 as reflections produced by a series of high– and low–wave speed layers at depths of 70 to 82 km in the upper mantle of the subducting Pacific Plate in New Zealand (Figs. 1B and 6). Because of the great depth of the reflections, and the smaller thicknesses of the layers, these moveout changes are necessarily subtle and can be emergent in long-offset data. Although our interpretation cannot be regarded as unique in all its details, the first-order
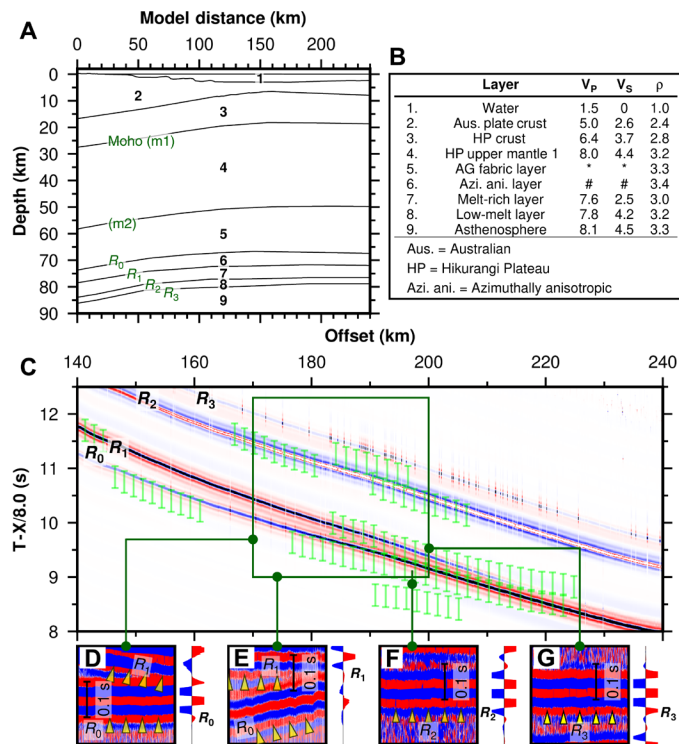
Fig. 5. Common receiver gathers from synthetic seismogram modeling. (**A**) Two-dimensional subsurface model used to calculate synthetic common receiver gather at the BFZ station with SAHKE01 airgun sources. (**B**) Table of velocity and density parameters of the subsurface model in (A). Elastic coefficients of the AG fabric are from (*20*). Density normalized elastic coefficients (in km²/s²) of the azimuthally anisotropic layer indicated by # in Voigt index notation (diagonally symmetric): $C_{11} = 87.00$, $C_{12} = 22.62$, $C_{13} = 24.38$, $C_{14} = -0.42$, $C_{15} = -4.36$, $C_{16} = 1.39$, $C_{22} = 72.41$, $C_{23} = 23.96$, $C_{24} = -0.27$, $C_{25} = 0.10$, $C_{26} = 0.93$, $C_{33} = 69.96$, $C_{34} = -0.27$, $C_{35} = -3.89$, $C_{36} = 0.28$, $C_{44} = 22.68$, $C_{45} = 0.79$, $C_{46} = -1.47$, $C_{55} = 26.87$, $C_{56} = -0.72$, and $C_{66} = 24.50$. (**C**) Synthetic common receiver gather from ANRAY. Note that the merging of R_0 and R_1 reflections at offsets of 190 to 200 km can be replicated only when the elastic tensor defining the velocities in the azimuthally anisotropic layer is rotated by 10° to 30° clockwise around the vertical axis (true azimuth of 322° to 342°) (figs. S8 to S19). The green rectangle indicates the region of the gather used in (D) to (G) to flatten R_0 to R_3 reflections horizontally using the travel time at each trace (left). The traces on the right in (D) to (G) are the stacked traces from the flattened traces (left). The first breaks of the arrivals are labeled. These stacks should be compared to those from the data shown in Fig. 2 (B to E).

structural configuration in which a thin, high-velocity layer overlies a thicker low-velocity layer is a model that best fits our observations.

DISCUSSION

We interpret the presence of a LAB zone (LABZ) at the base (≈70-km deep) of the Pacific Plate at the Hikurangi subduction margin in New Zealand. It consists of a 3 (±1)–km-thick azimuthally anisotropic layer overlying a low–P-wave speed layer of thickness 9 ± 2 km (Fig. 6). This layering is a natural up-dip continuation of the proposed LAB channel from an earlier on-land study based on near-vertical reflections (*10*). In this study, we resolve more details of the newly defined LABZ by analyzing wide-angle reflections that show a broader range of moveouts and amplitude variations than can be recorded by near vertical reflections.
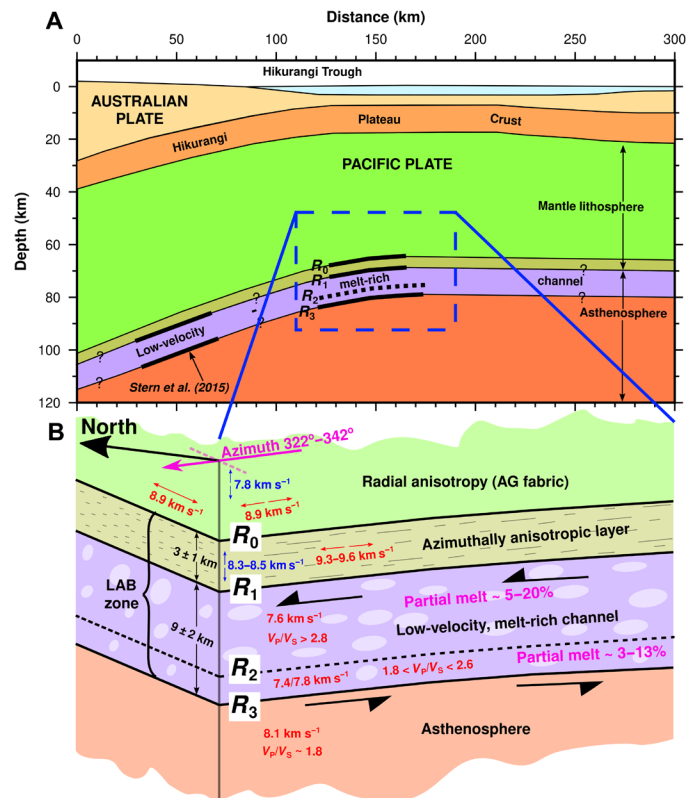

Fig. 6. Conceptual model of the lithosphere-asthenosphere boundary zone. (**A**) Schematic diagram of the LAB zone at the Hikurangi margin. The dashed rectangle indicates the extents of (B). (**B**) Interpretation of the observed anisotropic and low-velocity layers in the LAB zone. Colored labels indicate seismic P-wave velocities and V_P/V_S ratios.

Synthetic seismogram modeling suggests that the fast direction of the topmost layer of the LAB zone with V_P = 9.3 to 9.6 km/s lies along an azimuth between 322° and 342°, which is subparallel to the direction of absolute plate motion of the Pacific Plate at the Hikurangi margin (Fig. 1A) (*27*). A P-wave velocity of 8.3 to 8.5 km/s in the vertical (perpendicular) direction (Fig. 6 and figs. S8 to S19) is implied within this top layer. This layer effectively marks a change from radial (*20*) to azimuthal anisotropy (Fig. 6B). The high P-wave speeds would in part be due to the adoption of high wave speeds of 8.9 km/s at depths of 70 km, and our assumption that they, and the AG fabric they represent, extend to the base of the Pacific Plate. There could, however, be a low-velocity layer (V_P, ≈8.3 km/s) in between the AG fabric and the base of the plate, but the P-wave speed in the azimuthally anisotropic layer would still be required to be ≈9.3 km/s to fit the observed moveout of R_1 (figs. S26 and S27). Furthermore, in the common receiver gathers, there is no evidence between P_{n2} and R_0 arrivals for wide-angle reflections that might reflect the presence of such a low-velocity layer (V_P, ≈8.3 to 8.7 km/s) (Fig. 2).

The lowermost layer of the LABZ is interpreted to be a 9 (±2)–km-thick, low–P-wave velocity layer (Fig. 6). The high V_P/V_S ratios (>2.8) required in the upper part (7 ± 2 km) of this layer indicate a high fluid content (*28*), possibly reflecting the accumulation of melts (*29*). The relatively lower V_P/V_S ratios (1.8 to 2.6) in the lower part (2 ± 1 km) indicate a lower fluid content compared to the upper portion. Although our AVO modeling indicates that V_P/V_S ratios of

≈1.8 can explain the negative polarity of R_2 reflection with reflection coefficients of ≈0.2 for V_P ≈7.3 km/s (fig. S25), it may not be consistent with the lower reflection amplitudes of the R_2 reflector (<0.1). This 9 (±2)–km-thick, low V_P layer with high V_P/V_S ratios is interpreted to be the LAB channel of the Pacific Plate as it is consistent in its physical characteristics with the down-dip extension of the same low V_P, melt-rich, low-viscosity channel with high strain rates found under the North Island of New Zealand (Fig. 6) (10). The depth of this low-velocity layer also agrees well with the 70- to 80-km depth of the LAB channel for a 120-million-year-old oceanic plate (2, 6).

Low-velocity zones detected in the oceanic lithosphere have also been attributed to lenses of frozen melts (30), referred to as oceanic midlithospheric discontinuities (MLDs). They are proposed to contain wehrlite formed by the crystallization of MORB (mid-ocean ridge basalt)-type melts (30), which typically would have V_P/V_S ratios <1.8 (31). We do not ascribe the reflectivity that we observe to be from an MLD, as the high V_P/V_S ratios suggest the presence of melts.

The high V_P/V_S ratio of the top 7 ± 2 km portion of the low–P-wave velocity channel indicates a shear-wave velocity drop of about 40%. It represents ≈15% partial melt if melt is distributed in tubules (32), ≈20% partial melt assuming equilibrium melt geometries, or 5% partial melt if melt exists in thin films (33). Similarly, for the lower ≈2 ± 1 km, assuming a mean V_P/V_S ratio of 2.2, the estimated partial melt contents for the above melt geometries are ≈9% (tubules), ≈13% (equilibrium), and ≈3% (films).

The partial melt content of the LAB channel further down-dip of the Hikurangi subduction zone is estimated to be about 2% on the basis of the P-wave velocity reduction of 8 to 10% (10). Moreover, partial melt content in the LAB channel in the younger oceanic lithosphere near the Mid-Atlantic Ridge is estimated to be 1 to 5.5% from magnetotelluric data and receiver function modeling (9, 13). First, we suggest that our higher partial melt estimates may reflect the V_P/V_S ratio providing more realistic estimates on melt content, as S-waves are more sensitive to the presence of fluids. Last, we suggest that our higher partial melt estimates, compared to other tectonic settings, reflect a higher degree of melt accumulation at the flexed base of the lithosphere that forms as it bends due to subduction (34, 35), usually evidenced as bright, low-velocity LAB patches in seismic images (36, 37). These accumulated melts may also be the source of petit-spot volcanism observed in proximity to other subduction zones (34).

Partial melt fractions >5% can reduce the mantle viscosity by an order of magnitude (38) and, therefore, can decouple the lithosphere from the underlying mantle flow and facilitate plate tectonics to be possible. The presence of such melt fractions is consistent with modeling of seismic anisotropy and plate velocities (39). However, localized reductions in viscosity by thin isolated patches of high melt fraction would not affect global plate motions (39). With our study, we have detected the LAB at a subduction zone where it undergoes a downward bend, and hence, this may be a local feature and not indicative of ubiquitous melt beneath the oceanic lithosphere. Moreover, melt channels at the LAB may well be dynamic features that evolve over geologic time scales (9).

If seismic anisotropy is developed because of the resistive drag of the sublithospheric mantle, the strain will be localized in a horizontal shear zone several tens of kilometers thick between the rigid lithosphere and the asthenosphere (25). More importantly, melt accumulation and channelization at the LAB can cause strong strain localization (40). For example, a melt fraction of 4% can enhance the strain rate by a factor of ≈3 relative to that of melt-free upper mantle rocks (38), whereas a melt fraction of 7% that falls within our partial melt content estimates for the LAB channel can enhance the strain rate by a factor of ≈25 (38). Regions deforming at faster strain rates allow for increased alignment of the predicted fast azimuth of mantle olivine with the plate motion direction (41). We therefore suggest that the localization of strong azimuthal anisotropy in a 3-km-thick layer identified above the LAB channel in this study is the result of the lattice-preferred orientation of olivine crystals in response to the increased strain rates by melt accumulation at the base of the lithosphere.

Early long-offset seismic reflection and refraction studies (42–46) also pointed to the existence of high V_P, anisotropic layers at depths of 60 to 100 km in the upper mantle of both continents and oceans. Anisotropy detected in these studies is confined to layers that are less than 5 km thick and are separated by 10- to 20-km-thick low-velocity layers interpreted to reflect shear zones (45). One of these studies proposes a ≈5-km-thick anisotropic layer with a P-wave velocity of 8.5 km/s at depths near the LAB (46), and they propose that differential horizontal motion between the lithosphere and the asthenosphere has resulted in the lattice preferred orientation of mantle olivine. Our new results corroborate this view as this boundary zone between the lithosphere and the asthenosphere is clearly one of the most pervasive shear zones within the Earth, capable of accumulating large finite shear strains.

Our study highlights the potential and importance of wide-angle seismic reflections to explore the fine-scale structure and anisotropy of the upper mantle. Multichannel seismic (MCS) reflection surveys are capable of detecting a low-velocity layer at the base of the lithosphere (11), but they will struggle to detect azimuthally anisotropic, high–wave speed layers as the near-vertical raypaths induce only small amplitude reflections. Onshore-offshore seismic surveys and ocean bottom seismic surveys with long source-receiver offsets and tuned-airgun sources are favorable methods to explore fine-scale layering and anisotropy at LAB depths. Although the acquisition of new wide-angle data for investigating the LAB is challenging, we suggest that careful inspection and analysis of similar data already available may reveal intriguing facts about the LAB.

In summary, the LAB cannot be simply explained by a single low-velocity, melt-rich channel, as suggested from previous studies (6, 10, 11). Rather, it is a complex system of layers, including a low-velocity zone, which we term the LABZ.

MATERIALS AND METHODS
Structure of the Pacific Plate at the Hikurangi margin
The Pacific Plate, which contains the oceanic Hikurangi Plateau (47, 48), subducts beneath the Australian Plate at the east coast of the North Island of New Zealand (Fig. 1A). It moves with an absolute plate motion vector of 45 to 60 mm/year at an azimuth of ≈325° (27) and a relative plate motion vector (with respect to the Australian Plate) of ≈45 mm/year at an azimuth of ≈260° (Fig. 1A) (49). The depth to the base of the Pacific Plate under the southern North Island is estimated to be about 73 km from onshore explosions (10). The upper 10 to 12 km of the plate comprises the crust of the Hikurangi Plateau as suggested from controlled-source seismic data (14, 15, 50, 51). The bottom 60 km is taken up by the lithospheric mantle, which transitions into the asthenosphere through a ≈10-km-thick, low-velocity, sheared melt-rich layer interpreted as the LAB channel (10).

Controlled-source seismic data

The controlled-source seismic data used in the study are from the SAHKE conducted in the southern Hikurangi margin in 2009–2010 (*15*). During this experiment, SAHKE and PEGASUS MCS lines were acquired by *R/V Reflect Resolution* (Fig. 1B). The airgun source of the seismic vessel had a capacity of 98.3 liters (6000 in^3) for the SAHKE lines and a source spacing of 100 m. These parameters were reduced to 88.5 liters (5400 in^3) and 37.5 m for the PEGASUS lines. The source was towed at a depth of 6 ± 1 m for both configurations. Simultaneously, the airgun sources were recorded by a network of temporary seismographs and the permanent seismographs of the GeoNet network. For this study, we used airgun sources from SAHKE01 and PEGASUS23 lines recorded by onshore seismographs (Fig. 1).

The technique of using offshore airgun sources recorded at onshore receiver seismographs is known as the "onshore-offshore" method (*16*). Onshore-offshore seismic data are visualized using common receiver gathers. Common receiver gathers are produced by extracting seismograms from the continuously recorded data at the seismographs using GPS-located ship airgun source times and plotting them with source-receiver offset.

We further processed the common receiver gathers using GLOBE Claritas to enhance the signal-to-noise ratio. Processing included the following: a zero-phase band-pass filter with 2-4-8-15-Hz corner frequencies; an FK (frequency-wavenumber) filter to suppress noise; runmixing (horizontal trace averaging) and semblance coherency filtering to improve trace-to-trace coherency; and an automatic gain control of 10 s.

Wide-angle reflections in the onshore-offshore common receiver gathers

The common receiver gathers at BFZ and MRZ broadband seismographs of the GeoNet network (Fig. 1B), produced using the airgun sources of the SAHKE01 line and, at MRZ, produced using the airgun sources of the PEGASUS23 line, display several distinct seismic phases at two-way travel times >30 s and source-receiver offsets >140 km (Fig. 2 and figs. S1 to S3).

In the common receiver gathers at BFZ and MRZ stations with the airgun sources of the SAHKE01 line, we identify a band of reflectivity spanning ≈3.5 s at offsets ranging from ≈140 to 260 km. These occur at reduced travel times of 8 to 13 s (reduction velocity of 8 km/s) or true travel times of about 30 to 40 s. Within the coda of this reflectivity, several wide-angle reflections (R_0, R_1, R_2, and R_3) can be observed, more clearly in the gather at BFZ (Fig. 2A and fig. S2) and less clearly in the gather at MRZ (Fig. 2F and fig. S3). However, in the common receiver gather at the MRZ station with the airgun sources of PEGASUS23 line, weak reflection signals (R_1 and R_2) can be observed (Fig. 2G). R_1 and R_2 in this gather have lower amplitudes, possibly due to the less powerful airgun source used in the PEGASUS23 line.

Alternative explanations to the wide-angle reflections

We tested alternative models that may explain the characteristics of these late arriving phases (e.g., larger travel times and moveouts). These phases arrive after the P_{n2} phase, which is a refracted phase from a faster upper mantle layer with a P-wave speed of 8.7 ± 0.2 km/s at a depth of ≈50 km in the upper mantle of the Pacific Plate (*14*). The parabolic shape of these late arriving phases suggests that they are wide-angle reflections rather than refractions. Furthermore, the source-receiver offsets at which they are observed confirm that

they are reflections because the shortest source-receiver offsets of these phases (140 to 160 km) are less than the critical distance of ≈200 km for a refracted arrival from a ≈60-km-deep layer.

We tested the possibility of R_0, R_1, and R_2 being peg-leg multiples of the P_{n2} upper mantle refraction, within prominent reflectors in the sedimentary column. For this, the prominent reflectors in the MCS reflection data of the SAHKE01 line were mapped and depth converted. Travel-time picks of R_0, R_1, and R_2 were ray-traced using RAYINVR (*52*) with the raypaths defined as peg-leg multiples in between reflectors A and B (figs. S28 and S29). The calculated travel times could not fit the observed travel times at the maximum offsets unless the rays bounced back and forth between the A and B reflectors up to three and seven times. This is an unlikely scenario as the amplitudes decay substantially in between such reflections, and we would have expected to see earlier modes of such multiples at the same offsets. Furthermore, the calculated travel times could not account for the observed moveouts of the phases.

Next, we tested whether these phases could be explained by a P-wave–to–S-wave conversion where the P-wave from the airgun source arrives at the seismograph as an S-wave after converting at an interface along its way. For this, the north and east components of the seismograms for each airgun source were rotated to radial and transverse components, and the particle motion between different components was plotted. The particle motion diagrams indicate prominent polarization in the vertical component (figs. S30 and S31) and therefore the arrivals are most likely P-waves, and not S-waves arriving at the onshore seismograph. These particle motion diagrams also suggest that these arrivals are not a result of a sideswipe (e.g., from a fault zone and vertical crack) as it would also require the particle motion to have strong horizontal components.

These arrivals are recorded at two permanent seismographs of the GeoNet network, but not on the short-period temporary stations of SAHKE that were recording during this time. This may be a result of the permanent broadband stations being better coupled to the ground than the temporary stations. Furthermore, the permanent seismographs, MRZ and BFZ, are stationed on firm greywacke basement rocks compared to the temporary stations, which were located on a variety of surface rocks. We also cannot rule out the limited station observations of late-arriving wide-angle reflections to be the result from strong lateral heterogeneity at the LAB.

2D and 3D seismic ray tracing

We used seismic ray tracing to estimate the depths and interval velocities of the layers defined by R_0, R_1, R_2, and R_3 wide-angle reflections. Our ray trace models are based on the 2D isotropic P-wave velocity models for the PEGASUS23 and PEGASUS25 transects of (*14*) that constrain the P-wave velocity structure down to a depth of ≈50 km. In projecting the airgun sources from the SAHKE01 line onto the PEGASUS23 and PEGASUS25 velocity models (Fig. 1B), the effect from the difference in water depths at the original source locations and the projected source locations on the travel times of the phases is considered negligible as the maximum travel-time delay induced is within the pick uncertainties of 0.2 s (figs. S32 and S33 and table S1). Using RAYINVR, the travel times of the wide-angle reflected phases were forward-modeled in a top-down approach to minimize the travel-time residuals (Fig. 4, figs. S6 and S23, and table S1).

The assumption of 2D raypaths and isotropic velocities in the upper mantle can affect the estimates on the layer thicknesses and

interval velocities determined from 2D ray tracing. Therefore, we used the ANRAY package (53) for ray tracing in 3D, which can include both isotropic and anisotropic media in the velocity model. Similar to 2D ray tracing, we forward-modeled the travel times of the wide-angle reflections (table S2) using a 3D Earth model created by extending the velocity model derived from 2D ray tracing (Fig. 5A) perpendicular to the vertical plane for ANRAY.

The ability to incorporate anisotropic media defined by elastic tensor coefficients in ANRAY is an advantage as the lithospheric mantle consists of anisotropic minerals, predominantly olivine. The elastic tensor for pure forsterite olivine (Mg_2SiO_4) at 2.5 GPa, corresponding to a depth of 70 to 80 km in the lithospheric mantle, was obtained by the linear interpolation of the elastic tensor coefficients (54). Using this, the elastic tensor for aggregates of forsterite crystals with their crystallographic axes oriented in different directions was obtained from MTEX MATLAB Toolbox (55) and was incorporated into ANRAY.

2D and 3D synthetic seismogram modeling

We used the ANRAY package (53), which uses a ray tracing–based method to calculate synthetic waveforms for the required wide-angle reflections in 3D. For this, we used the 3D Earth model created for 3D ray tracing. For isotropic layers, shear-wave velocities using appropriate V_P/V_S ratios between 1.8 and 3.0 and densities were used (Fig. 5, A and B). Instead of recording a number of marine sources by a seismograph onshore, the computations were made efficient by replacing the onshore receiver by a point source and marine airgun sources by a linear array of receivers in water as reciprocity is valid for synthetic seismogram modeling (56). Thus, synthetic common receiver gathers were produced by plotting the seismograms with source-receiver offset. The resulting synthetic seismograms were convolved with the source-time function of the airgun array of *R/V Reflect Resolution*.

AVO modeling

The Zoeppritz equations for partitioning of seismic displacements at an interface provide information linking polarity and amplitude of a reflection with offset (or incident angle) to the impedance contrast across the interface (57). We used them to search for the impedances (V_P, V_S, and density) of the layers in a top-down approach assuming isotropic media (figs. S22 and S25). We also computed the reflection coefficients with offset for transversely isotropic (radially anisotropic) media using the equations of (58) in which the anisotropic parameters are defined by Thomsen's parameters (59), δ and ε (fig. S20).

Uncertainty/trade-off estimation

We used a perturbation test to estimate the uncertainty in the determination of the depth to the R_0 reflector (fig. S7) where the preferred depth of the reflector (70 km) was perturbed at regular intervals (1 km) and the resultant root mean square (RMS) travel-time misfit (T_{RMS}) was obtained from RAYINVR ray tracing. The 95% confidence interval was estimated, within which there is a 95% probability for the modeled depth to fit the observations (14). The uncertainty in the estimated depth of the R_0 reflector is ±1 km (fig. S7).

Estimation of the model parameter uncertainties and trade-offs based on travel-time misfits when anisotropy is considered does not provide clear results owing to the increased number of model parameters/variables. Therefore, to estimate the uncertainties in the thickness and velocities (thereby anisotropy) of the azimuthally anisotropic layer between R_0 and R_1, we calculated synthetic common receiver gathers using ANRAY for the following: layer thicknesses ranging from 1 to 4 km; a set of elastic tensors calculated using MTEX (55) for aggregates of forsterite crystals oriented in different directions; and different azimuthal orientations of the elastic tensors (312° to 362°). The converging nature of R_0 and R_1 at offsets between 190 and 200 km and the separation between them at offsets <190 km were used as a proxy to estimate the uncertainties in the thickness and velocities (figs. S8 to S19). The models that could replicate these features in the observed data are considered to represent the trade-offs between the velocities and thickness of this azimuthally anisotropic layer (figs. S8 to S19). The estimated trade-offs are 2 to 4 km in thickness and 9.3 to 9.6 km/s in the velocity of the fast direction oriented along azimuths between 322° and 342°.

We used grid search tests to estimate the trade-offs between the thicknesses and the P-wave velocities of the layers in between R_1 and R_2 and in between R_2 and R_3 reflections (fig. S24). Grid searches were carried out within probable model parameter values to minimize T_{RMS} using ANRAY to account for anisotropy. T_{RMS} appears to converge to a minimum value only with respect to the thickness of the layers (fig. S24). Therefore, we use 5 to 12% P-wave velocity reduction relative to a background asthenospheric P-wave velocity of 8.1 km/s as an estimate on the trade-off of the P-wave velocity within these two layers (fig. S24). With these constraints, conservatively, the uncertainties in the thickness and P-wave velocity of the layer between R_1 and R_2 reflections are estimated to be ±2 km and ±0.5 km/s, respectively (fig. S24A). Similarly, those of the layer between R_2 and R_3 reflections are ±1 km and ± 0.5 km/s, respectively (fig. S24B).

A limiting minimum V_P/V_S ratio of 2.8 for the low-velocity channel between R_1 and R_2 was obtained by searching for V_P/V_S ratios that could explain the positive polarity of the first break of R_1 within the incident angles obtained from ray tracing (fig. S21).

We also conducted grid searches for density, P-wave velocity, and V_P/V_S ratio combinations that could explain the positive and negative polarities of R_1 and R_2 reflections, respectively, within the range of incident angles to estimate the trade-offs in parameter estimations (figs. S22 and S25).

SUPPLEMENTARY MATERIALS

Supplementary material for this article is available at https://science.org/doi/10.1126/sciadv.abn5697

REFERENCES AND NOTES

1. R. M. Richardson, Ridge forces, absolute plate motions, and the intraplate stress field. *J. Geophys. Res. Solid Earth* **97**, 11739–11748 (1992).
2. K. M. Fischer, H. A. Ford, D. L. Abt, C. A. Rychert, The lithosphere-asthenosphere boundary. *Annu. Rev. Earth Planet. Sci.* **38**, 551–575 (2010).
3. C. A. Rychert, N. Harmon, S. Constable, S. Wang, The nature of the lithosphere-asthenosphere boundary. *J. Geophys. Res. Solid Earth* **125**, e2018JB016463 (2020).
4. S.-i. Karato, H. Jung, I. Katayama, P. Skemer, Geodynamic significance of seismic anisotropy of the upper mantle: New insights from laboratory studies. *Annu. Rev. Earth Planet. Sci.* **36**, 59–95 (2008).
5. C. A. Rychert, P. M. Shearer, K. M. Fischer, Scattered wave imaging of the lithosphere-asthenosphere boundary. *Lithos.* **120**, 173–185 (2010).
6. H. Kawakatsu, P. Kumar, Y. Takei, M. Shinohara, T. Kanazawa, E. Araki, K. Suyehiro, Seismic evidence for sharp lithosphere-asthenosphere boundaries of oceanic plates. *Science* **324**, 499–502 (2009).
7. P. Kumar, X. Yuan, M. R. Kumar, R. Kind, X. Li, R. K. Chadha, The rapid drift of the Indian tectonic plate. *Nature* **449**, 894–897 (2007).
8. C. A. Rychert, K. M. Fischer, S. Rondenay, A sharp lithosphere-asthenosphere boundary imaged beneath eastern North America. *Nature* **436**, 542–545 (2005).

9. C. A. Rychert, S. Tharimena, N. Harmon, S. Wang, S. Constable, J. M. Kendall, P. Bogiatzis, M. R. Agius, D. Schlaphorst, A dynamic lithosphere–asthenosphere boundary near the equatorial Mid-Atlantic Ridge. *Earth Planet. Sci. Lett.* **566**, 116949 (2021).

10. T. A. Stern, S. A. Henrys, D. Okaya, J. N. Louie, M. K. Savage, S. Lamb, H. Sato, R. Sutherland, T. Iwasaki, A seismic reflection image for the base of a tectonic plate. *Nature* **518**, 85–88 (2015).

11. F. Mehouachi, S. C. Singh, Water-rich sublithospheric melt channel in the equatorial Atlantic Ocean. *Nat. Geosci.* **11**, 65–69 (2018).

12. S. Naif, K. Key, S. Constable, R. L. Evans, Melt-rich channel observed at the lithosphere-asthenosphere boundary. *Nature* **495**, 356–359 (2013).

13. S. Wang, S. Constable, C. A. Rychert, N. Harmon, A lithosphere-asthenosphere boundary and partial melt estimated using marine magnetotelluric data at the central middle atlantic ridge. *Geochemistry, Geophys. Geosystems* **21**, e2020GC009177 (2020).

14. P. Herath, T. A. Stern, M. K. Savage, D. Bassett, S. Henrys, C. Boulton, Hydration of the crust and upper mantle of the Hikurangi Plateau as it subducts at the southern Hikurangi margin. *Earth Planet. Sci. Lett.* **541**, 116271 (2020).

15. S. Henrys, A. Wech, R. Sutherland, T. Stern, M. Savage, H. Sato, K. Mochizuki, T. Iwasaki, D. Okaya, A. Seward, B. Tozer, J. Townend, E. Kurashimo, T. Iidaka, T. Ishiyama, SAHKE geophysical transect reveals crustal and subduction zone structure at the southern Hikurangi margin, New Zealand. *Geochemistry, Geophys Geosystems* **14**, 2063–2083 (2013).

16. D. Okaya, T. Stern, S. Holbrook, H. van Avendonk, F. Davey, S. Henrys, Imaging a plate boundary using double-sided onshore-offshore seismic profiling. *Lead Edge* **22**, 256–260 (2003).

17. J. P. Castagna, Petrophysical imaging using AVO. *Lead Edge* **12**, 172–178 (1993).

18. P. Kearey, M. Brooks, I. Hill, *An Introduction to Geophysical Exploration* (Blackwell Science, ed. 3, 2002).

19. R. E. Sheriff, L. P. Geldart, *Exploration Seismology* (Cambridge Univ. Press, ed. 2, 1995; www.cambridge.org/core/books/exploration-seismology/CC00727A219943E62F6FF01426DBA9D2).

20. T. Stern, S. Lamb, J. D. P. Moore, J. D. P. Moore, D. Okaya, K. Hochmuth, High mantle seismic P-wave speeds as a signature for gravitational spreading of superplumes. *Sci. Adv.* **6**, eaba7118 (2020).

21. M. P. Chadwick, The 1991 Hikurangi Margin seismic refraction experiment. Thesis, Victoria University of Wellington (1997).

22. D. Eberhart-Phillips, S. Bannister, M. Reyners, S. Henrys, New Zealand Wide model 2.2 seismic velocity and Qs and Qp models for New Zealand [Dataset]. *Zenodo* (2020), doi:10.5281/ZENODO.3779523.

23. K. Michibayashi, D. Mainprice, A. Fujii, S. Uehara, Y. Shinkai, Y. Kondo, Y. Ohara, T. Ishii, P. Fryer, S. H. Bloomer, A. Ishiwatari, J. W. Hawkins, S. Ji, Natural olivine crystal-fabrics in the western Pacific convergence region: A new method to identify fabric type. *Earth Planet. Sci. Lett.* **443**, 70–80 (2016).

24. A. Tommasi, A. Vauchez, R. Russo, Seismic anisotropy in ocean basins: Resistive drag of the sublithospheric mantle? *Geophys. Res. Lett.* **23**, 2991–2994 (1996).

25. A. Tommasi, Forward modeling of the development of seismic anisotropy in the upper mantle. *Earth Planet. Sci. Lett.* **160**, 1–13 (1998).

26. B. L. N. Kennett, E. R. Engdahl, Traveltimes for global earthquake location and phase identification. *Geophys. J. Int.* **105**, 429–465 (1991).

27. C. Kreemer, Absolute plate motions constrained by shear wave splitting orientations with implications for hot spot motions and mantle flow. *J. Geophys. Res. Solid Earth* **114**, 1–18 (2009).

28. M.-W. Lee, Velocity ratio and its application to predicting velocities. *U.S. Geol. Surv. Bull.* **2197**, 19 (2003).

29. T. Sakamaki, A. Suzuki, E. Ohtani, H. Terasaki, S. Urakawa, Y. Katayama, K. Funakoshi, Y. Wang, J. W. Hernlund, M. D. Ballmer, Ponded melt at the boundary between the lithosphere and asthenosphere. *Nat. Geosci.* **6**, 1041–1044 (2013).

30. A. Ohira, S. Kodaira, Y. Nakamura, G. Fujie, R. Arai, S. Miura, Evidence for frozen melts in the mid-lithosphere detected from active-source seismic data. *Sci. Rep.* **7**, 15770 (2017).

31. B. R. Hacker, G. A. Abers, Subduction factory 3: An Excel worksheet and macro for calculating the densities, seismic wave speeds, and H_2O contents of minerals and rocks at pressure and temperature. *Geochemistry, Geophys. Geosystems* **5**, 10.1029/2003GC000614, (2004).

32. W. C. Hammond, E. D. Humphreys, Upper mantle seismic wave velocity: Effects of realistic partial melt geometries. *J. Geophys. Res. Solid Earth* **105**, 10975–10986 (2000).

33. A. N. Clark, C. E. Lesher, Elastic properties of silicate melts: Implications for low velocity zones at the lithosphere-asthenosphere boundary. *Sci. Adv.* **3**, e1701312 (2022).

34. N. Hirano, E. Takahashi, J. Yamamoto, N. Abe, S. P. Ingle, I. Kaneoka, T. Hirata, J.-I. Kimura, T. Ishii, Y. Ogawa, S. Machida, S. Kiyoshi, Volcanism in response to plate flexure. *Science* **313**, 1426–1428 (2006).

35. J. Yamamoto, J. Korenaga, N. Hirano, H. Kagi, Melt-rich lithosphere-asthenosphere boundary inferred from petit - spot volcanoes. *Geology* **42**, 967–970 (2014).

36. S. Aulbach, Cratonic lithosphere discontinuities, in *Lithospheric Discontinuities* (John Wiley & Sons, 2018), pp. 177–203.

37. W. B. Hawley, R. M. Allen, M. A. Richards, Tomography reveals buoyant asthenosphere accumulating beneath the Juan de Fuca plate. *Science* **353**, 1406–1408 (2016).

38. G. Hirth, D. L. Kohlstedt, Experimental constraints on the dynamics of the partially molten upper mantle: Deformation in the diffusion creep regime. *J. Geophys. Res. Solid Earth* **100**, 1981–2001 (1995).

39. T. W. Becker, Superweak asthenosphere in light of upper mantle seismic anisotropy. *Geochemistry, Geophys. Geosystems* **18**, 1986–2003 (2017).

40. S. C. Kruckenberg, B. Tikoff, V. G. Toy, J. Newman, L. I. Young, Strain localization associated with channelized melt migration in upper mantle lithosphere: Insights from the Twin Sisters ultramafic complex, Washington, USA. *J. Struct. Geol.* **50**, 133–147 (2013).

41. L. N. Hansen, C. Qi, J. M. Warren, Olivine anisotropy suggests Gutenberg discontinuity is not the base of the lithosphere. *Proc. Natl. Acad. Sci. U.S.A.* **113**, 10503–10506 (2016).

42. C.-E. Lund, The fine structure of the lower lithosphere underneath the blue road profile in northern Scandinavia. *Tectonophysics* **56**, 111–122 (1979).

43. K. Fuchs, Structure, physical properties and lateral heterogeneities of the subcrustal lithosphere from long-range deep seismic sounding observations on continents. *Tectonophysics* **56**, 1–15 (1979).

44. J. Díaz, J. Gallart, D. Córdoba, L. Senos, L. Matias, E. SuriÑach, A. Hirn, P. Maguire, A deep seismic sounding investigation of lithospheric heterogeneity and anisotropy beneath the Iberian Peninsula. *Tectonophysics* **221**, 35–51 (1993).

45. C. J. Bean, A. W. B. Jacob, P-wave anisotropy in the lower lithosphere. *Earth Planet. Sci. Lett.* **99**, 58–65 (1990).

46. A. Hirn, Anisotropy in the continental upper mantle: Possible evidence from explosion seismology. *Geophys. J. Int.* **49**, 49–58 (1977).

47. B. Taylor, The single largest oceanic plateau: Ontong Java–Manihiki–Hikurangi. *Earth Planet. Sci. Lett.* **241**, 372–380 (2006).

48. R. I. Walcott, Reconstructions of the New Zealand region for the Neogene. *Palaeogeogr. Palaeoclimatol. Palaeoecol.* **46**, 217–231 (1984).

49. C. DeMets, R. G. Gordon, D. F. Argus, Geologically current plate motions. *Geophys. J. Int.* **181**, 1–80 (2010).

50. B. Tozer, T. Stern, S. L. Lamb, S. A. Henrys, Crust and upper-mantle structure of Wanganui Basin and southern Hikurangi margin, North Island, New Zealand as revealed by active source seismic data. *Geophys. J. Int.* **211**, 718–740 (2017).

51. K. Mochizuki, R. Sutherland, S. Henrys, D. Bassett, H. van Avendonk, R. Arai, S. Kodaira, G. Fujie, Y. Yamamoto, N. Bangs, D. Barker, Recycling of depleted continental mantle by subduction and plumes at the Hikurangi Plateau Large igneous province, southwestern Pacific Ocean. *Geology* **47**, 795–798 (2019).

52. C. A. Zelt, R. B. Smith, Seismic traveltime inversion for 2-D crustal velocity structure. *Geophys. J. Int.* **108**, 16–34 (1992).

53. D. Gajewski, I. Pšenčík, Computation of high-frequency seismic wavefields in 3-D laterally inhomogeneous anisotropic media. *Geophys. J. Int.* **91**, 383–411 (1987).

54. C.-S. Zha, T. S. Duffy, R. T. Downs, H.-K. Mao, R. J. Hemley, Sound velocity and elasticity of single-crystal forsterite to 16 GPa. *J. Geophys. Res. Solid Earth* **101**, 17535–17545 (1996).

55. D. Mainprice, R. Hielscher, H. Schaeben, Calculating anisotropic physical properties from texture data using the MTEX open-source package. *Geol. Soc. London Spec. Publ.* **360**, 175–192 (2011).

56. H. Igel, *Computational Seismology: A Practical Introduction* (Oxford Univ. Press, ed. 1, 2016).

57. K. Aki, P. G. Richards, *Quantitative Seismology* (University Science Books, ed. 2, 2002).

58. J. P. Blangy, AVO in transversely Isotropic media—An overview. *Geophysics* **59**, 775–781 (1994).

59. L. Thomsen, Weak elastic anisotropy. *Geophysics* **51**, 1954–1966 (1986).